Supporting Information

An ion sieve-tailored biomimetic porous nanofibrous as an efficient adsorbent for lithium extraction from brine

Xiulei Li, Zhihui Wang, Hexin Zhang, Wen Zhang, Jiacun Jiang, Ruili Guo*

School of Chemistry and Chemical Engineering/Key Laboratory for Green Processing of Chemical Engineering of Xinjiang Bingtuan, Shihezi University, Shihezi, Xinjiang, 832003, China

Corresponding author: *R. Guo.

Tel.: 86-993-2057006.

Fax: 86-993-2057210.

E-mail address: grli@shzu.edu.cn.

Contents

Keywords: Lithium-ion sieves; $Li_{1.6}Mn_{1.6}O_4$ crystallites; Porous nanofibers structures; Lithium recovery; Brine water

1. Experiments

S1. Materials

Ammonium hydroxide ($NH_3 \cdot H_2O$, 25-28%), manganese acetate ($Mn(CH_3COO)_2 \cdot 4H_2O$, ≥99.0%), ammonium chloride (NH_4Cl), Lithium perchlorate ($LiClO_4$, ≥98.0%) were purchased from Tianjin Beilian Reagent Co., Ltd. Methyl alcohol (CH_3OH, ≥99.5%) and acetic acid (CH_3COOH, ≥99.5%) was purchased from Tianjin Fuchen Chemical Reagents Factory. Hydrochloric acid (HCl, 36-38%) was purchased from the Chengdu Kelong Chemical Reagent Factory. Lithium chloride monohydrate ($LiCl \cdot H_2O$, ≥99.5%) potassium chloride (KCl, ≥99.5%), calcium chloride anhydrous ($CaCl_2$, ≥99.5%), sodium chloride (NaCl, ≥99.5%), magnesium chloride hexahydrate ($MgCl_2 \cdot 6H_2O$, ≥99.5%) were purchased from Tianjin Shengao Chemical Reagent Co., Ltd. Polyvinylpyrrolidone (PVP, Mw≈1,300,000 $g \cdot mol^{-1}$) was purchased from Macklin.

S2. Preparation of lithium-ion sieve with porous nanofiber structure

Lithium-ion sieve with a porous nanofiber structure was prepared by electrospinning technology, high-temperature calcination and ion exchange with hydrochloric acid. Take the preparation process of NFs@LIS-6:6 as an example, the specific preparation process is as follows: 6wt% polyvinylpyrrolidone (PVP) powder and 6wt% metal salt (comprised of $LiClO_4$ and $Mn(CH_3COO)_2 \cdot 4H_2O$ composition, stoichiometric ratio 1:1) dissolve in a spinning solution by mixing 18 mL methanol with

1.5 mL glacial acetic acid and stirring it continuously for 5 h. The electrostatic spinning equipment was used to prepare nanofiber membranes. We calcined the nanofibers at 500 °C in a muffle furnace with a heating rate of 0.5 °C·min^{-1} for 4h and named them NFs@LMO-X:Y (X=6, Y=6) , where X was the high molecular content and Y was the metal salt content. Finally, after acid treatment (0.5 mol·L^{-1} HCl), the porous nanofiber lithium-ion sieve was obtained and named NFs@LIS-X:Y (X=6, Y=6), where X was the high molecular content and Y was the metal salt content. Under similar experimental conditions, besides NFs@LIS-6:6 preparation, in the synthesis of NFs@LIS-6:1, NFs@LIS-6:3, NFs@LIS-6:12, NFs@LIS-9:1, NFs@LIS-9:3 and NFs@LIS-9:6, respectively. The mass percentages of polymer, metal salt and solvent in each spinning solution are shown in Table S1.

S3. Setting parameters of electrospinning equipment

The lithium-ion sieve is prepared by a combination of electrostatic spinning technology and high-temperature calcination. The mass percentages of polymer, metal salt and solvent in each spinning solution are shown in Table S1. A stainless-steel needle, anode, needle 24G, diameter 0.27 mm, was attached to a 5 mL plastic syringe containing the solution. The tip of the nozzle is positioned 12 cm from the metal cathode (collector). Spinning conditions: positive voltage 12 kV, negative voltage 2 kV, push column speed 1.0 mL·h^{-1}, drum receiving, receiving speed 60.0 r·min^{-1}, relative humidity and temperature are 20% and 35 ℃, parallel displacement is ± 4 cm, the stroke is 15 mm, and the translation speed is 400 mm·min^{-1}.

S4. Characterization

Porous nanofibers ($Li_{1.6}Mn_{1.6}O_4$) have been characterized by X-ray diffraction (XRD, D8 Advanced, Cu-K, 40 kV, 40 mA) at a scan speed of $2°\cdot min^{-1}$. Morphology and composition of the obtained samples were determined by scanning electron microscope (SEM, JSM-6490LV) and transmission electron microscope (TEM, FEI TALOS F200) equipped with X-ray dispersive spectroscopy (EDS). An analysis of TGA was conducted under air at a heating rate of 10 $°C\cdot min^{-1}$ at temperature ranges between 50 and 800 °C. The valence of Mn of porous nanofibers ($Li_{1.6}Mn_{1.6}O_4$) was analyzed by X-ray photoelectron spectroscopy (XPS, K-α 1486.6, Thermo ESCALAB 250xi). Analyzing the chemical structure was carried out using a fourier transform infrared spectrometer (FTIR, AVATAR 360, Nicolet, USA) measuring range 400-4000 cm^{-1} with a resolution of 2 cm^{-1}. With an atomic absorption spectrophotometer (AA7003, East and West Analysis, China), the metal ions (Li^+, Na^+, K^+, Ca^{2+}, Mg^{2+}) concentration in the solution was measured.

S5. Li^+ adsorption performance measurements

The Li^+ adsorption performance of the lithium-ion sieve was tested, including the lithium solution adsorption performance test and simulated brine lithium extraction performance test, which is consistent with the results described in our previous study [36]. Section S6~S9 introduces the lithium solution adsorption performance test and simulated brine lithium extraction performance test, as well as the detailed operating procedures.

S6. Li^+ adsorption performance of lithium-ion sieves

LIS (10 mg) was dispersed in a LiCl-NH_4Cl-$NH_3\cdot H_2O$ buffer solution (10 mL, pH

= 9.8±0.1, Li^+ concentration = 50 mg·L^{-1}) at 30 °C and stirred (150 r·min^{-1}) for 12 h. The adsorption capacity of Li^+ (Q) was calculated by the following equation:

$$Q = \frac{(C_0 - C) \times V}{m} \quad (1)$$

where Q is the adsorption capacity, mg·g^{-1}; C_0 is the initial concentration of lithium in the solution, mg·L^{-1}; C is the lithium concentration after the adsorption, mg·L^{-1}; V is the volume of the solution, L; and m is the mass of the LIS, g.

S7. Adsorption kinetics studies

LIS (10 mg) was dispersed in a LiCl-NH_4Cl-$NH_3 \cdot H_2O$ buffer solution (10 mL, pH = 9.8±0.1, Li^+ concentration = 50 mg·L^{-1}) at 30 °C and stirred (150 r·min^{-1}) for 12 h. The experimental data were fitted with a pseudo-first-order kinetics model (Eq. 2) and a pseudo-second-order kinetics model (Eq. 3):

$$\ln(Q_e - Q_t) = \ln Q_e - k_1 t \quad (2)$$

$$\frac{t}{Q_t} = \frac{1}{Q_e^2 k_2} + \frac{t}{Q_e} \quad (3)$$

where Q_e is the equilibrium adsorption capacity of LIS, mg·g^{-1}; Q_t is the adsorption capacity of LIS at a certain time, mg·g^{-1}; k_1 is the rate constant for the pseudo-first-order model, h^{-1}; and k_2 is the rate constant for the pseudo-second-order model, g·mg^{-1}·h^{-1}.

S8. Adsorption isotherm studies

LIS (10 mg) was dispersed in a LiCl-NH_4Cl-$NH_3 \cdot H_2O$ buffer solution (10 mL, pH = 9.8±0.1) at 30 °C and stirred (150 r·min^{-1}) for 12 h. The initial concentration was adjusted from 25 mg·L^{-1} to 200 mg·L^{-1}. The results were fitted by the Langmuir model

(Eq.4) and the Freundlich model (Eq. 5):

$$\frac{C_e}{Q} = \frac{C_e}{Q_m} + \frac{1}{Q_m \cdot K_L} \quad (4)$$

$$\log Q = \frac{1}{n}\log C_e + \log K_F \quad (5)$$

where Q_e is the equilibrium adsorption capacity of LIS, mg·g^{-1}; C_e is the equilibrium concentration, mg·L^{-1}; Q_m is the maximum adsorption capacity of LIS, mg·g^{-1}; K_L is the Langmuir isotherm constant, L·mg^{-1}; and n and K_F are Freundlich constants, indicating the relative adsorption capacity and adsorption intensity, respectively.

S9. Adsorption circularity and selectivity studies

Determine the adsorption capacity of the adsorbent according to the method of S6 adsorption performance test. LIS was dispersed in a LiCl-NH_4Cl-$NH_3 \cdot H_2O$ buffer solution (pH = 9.8±0.1, Li^+ concentration = 250 mg·L^{-1}) at 30 °C and stirred (150 r·mi^{n-1}) for 12 h. After the adsorption, wash the adsorbed adsorbent to neutral with deionized water and use it for the next desorption. The desorption conditions are 150 r·min^{-1} and 30 ℃. Use 0.5 mol·L^{-1} HCl in a thermostatic oscillator for desorption. After desorption, take the supernatant and filter it with a filter membrane for collection, measure the lithium ion concentration of the solution to be measured, and calculate the desorption amount. Every 12 h is a cycle, so repeat. The calculation formula of desorption is

$$Q_{des} = \frac{C_{des} \times V'}{m'} \quad (6)$$

where Q_{des} is the desorption capacity, mg·g^{-1}; C_{des} is the concentration of lithium in the desorption solution, mg·L^{-1}; V′ is the volume of desorption solution, L; m' is the

mass of LIS adsorbent after adsorption and recovery, g.

LIS (10 mg) was dispersed in simulation brine (10 mL, pH = 7.3±0.1) at 30 °C for 12 h. The distribution concentration, K_d; separation coefficient, αLi Me; and concentration factor, C_F were calculated using the following equations:

$$K_d = \frac{(C_o - C_e) \times V}{m \times C_e} \quad (7)$$

$$\alpha_{Me}^{Li} = \frac{K_d(Li)}{K_d(Me)},\ Me\text{: } Li,\ Na,\ K,\ Mg \text{ and } Ca \quad (8)$$

and

$$C_F = \frac{Q_e(Me)}{C_o(Me)} \quad (9)$$

where Q_e is the equilibrium adsorption capacity of LIS, mg·g^{-1}; C_e is the equilibrium concentration, mg·L^{-1}; C_o is the initial concentration of metal ions in simulation brine, mg·L^{-1}; V is the volume of the solution, mL; and m is the LIS mass, g.

S10. Effect of metal salt and polymer content on crystal form and structure of the precursor

The results of the X-ray diffraction patterns of different samples are shown in Figure S1. All diffraction peaks correspond to the standard PDF card of $Li_{1.6}Mn_{1.6}O_4$ (PDF#52-1841). They all presented characteristic peaks of 18.8°, 36.5°, 44.5°, 58.9° and 64.7°, corresponding to the spinel $Li_{1.6}Mn_{1.6}O_4$ (111), (311), (400), (511) and (440) crystals. The surface corresponds to the spinel-type $Li_{1.6}Mn_{1.6}O_4$ (space group: Fd3m). The main characteristic diffraction peaks first increase and then decrease with the increase of the amount of metal salt, the strongest characteristic peak is provided by NFs@LMO-6:6. This phenomenon could be explained by the nucleation theory of the crystal. When the

amount of metal salt is less, the degree of supersaturation is low. Lithium perchlorate, manganese acetate, and PVP undergo decomposition, and transition products are formed, resulting in the nucleation of the crystal being slower, the crystal grains being larger, and the peaks broadened; when the dosage increases, the supersaturation increases, the nucleation speed increases, the crystal grains are smaller, and the characteristic peak intensity is greater; but when the dosage is too large, the viscosity of reaction system increases, the molecular diffusion is slower, the nucleation speed decreases, and the crystallinity is poor. Therefore, the amount of metal salt in the spinning solution is too much or too little is not suitable, and it is found that the highest crystalline LMO is obtained when the content of metal salt is 6wt%.

To explore the evolution mechanism of the morphology of nanofibers with different component ratios in the spinning solution after high-temperature calcination, the thermal behavior and morphology of nanofibers with different components were studied and characterized by SEM. Figure S2 showed the scanning electron micrograph of nanofibers prepared before and after calcination at 500 ℃. It can be seen from the figure that as the mass ratio of PVP and metal salt in the precursor changed, the morphology of $Li_{1.6}Mn_{1.6}O_4$ nanofibers also changed. NFs@LMO-6:1 is assembled into a loose structure. With the increase of metal salt content, NFs@LMO-6:6 ($Li_{1.6}Mn_{1.6}O_4$) showed uniform nanoparticles, no pores and microspheres, and the structure is more compact. However, with the continuous increase of metal salt content, some grains are more or less convex on the surface of nanofibers with 12wt% metal salt content after heat treatment at 500 ºC, resulting in an uneven surface. The results

show that uniform porous nanofibrous $Li_{1.6}Mn_{1.6}O_4$ can be obtained by using appropriate PVP and metal salt mixed precursor solution, the comprehensive results show that the optimum content of metal salt is 6wt%.

Based on previous studies, the effects of high molecular content on the structure and crystal form of precursors were further discussed. The SEM images of nanofibers prepared after increasing the high molecular content to 9wt% before and after calcination are shown in Figure S3. The nanofibers have retained their three-dimensional nanofiber skeleton structure before calcination with increasing polymer content. After calcination at 500 °C for 4 h at a rate of 0.5 ℃·min^{-1}, when the additional amount of metal salt is only 1wt%, the calcined product showed sheet structure with a small amount crystalline nanoparticals inside. This is because the thermal decomposition of the polymer and the content of metal salt is less. The nanoparticles inside are scarce and not enough to connect, the residual carbon skeleton too less to maintain an independent nanofiber morphology, result the nanofiber showing a molten morphology.

Figure S3 (h-l) shows the SEM image of lithium-ion sieve precursor obtained from the calcination of nanofiber membrane with PVP content of 9wt% at different heating rates. Namely, calcination at different heating rates yielded SEM images of NFs@LMO-9:6. The calcination procedure is as follows: calcine at 500 ℃ for 4h in an air atmosphere at a heating rate of 0.5 ~ 5 ℃·min^{-1}. It can be seen that in the polymer system, with the decrease in heating rate, the polymer gradually decomposes, the nanoparticles gradually form, and the nanofiber roots gradually appear. Schematic

diagram of morphology evolution with the decrease of the heating rate is shown in Figure S5. The experimental results show that the slow heating rate is helpful to maintain the original shape of the sample.

Moreover, the XRD pattern (Figure S4) shows that the spinel structure of $Li_{1.6}Mn_{1.6}O_4$ remains unchanged despite reducing the heating rate. However, with the deepening of research, when the mass fraction of polymer is 9wt%, with the increase of metal salt content, the morphology of porous nanofiber skeleton is gradually clear under the same conditions. When the mass fraction of metal salt is 1wt%, as the polymer mass fraction increases from 6wt% to 9wt%, the morphology of the porous nanofiber skeleton become rough. When the addition amount of metal salt is 3wt%, due to the increase of high molecular weight content from 6wt% to 9wt%, the carbon residue of calcined nanofibers is relatively high, and the excess nanoparticles formed by metal salt crystals precipitates adhering to its surface rather than retained inside, resulting in rough and uneven distribution. This is also proved under the condition that the addition amount of metal salt is maintained at 6wt%. Therefore, the final investigation concluded that the high molecular weight content of 6wt% is more appropriate.

Figure S6 (a) shows the NFs@LMO-6:6 XRD pattern of lithium-ion sieve precursors synthesized by precursor nanofibers after different calcination times. These samples calcine at 600 ℃ in air atmosphere for 4 h, 6 h and 8 h respectively. It can be seen from the figure that all NFs@LMO show characteristic peaks at 18.8°, 36.5°, 44.5°, 58.9° and 64.7°, corresponding to spinel $Li_{1.6}Mn_{1.6}O_4$ (111), (311), (400), (511) and (440) crystal planes. With the increase in calcination time, the characteristic peak intensities

of $Li_{1.6}Mn_{1.6}O_4$ at 18.8°, 36.5°, 44.5°, 58.9° and 64.7° showed a trend of weakening first and then strengthening. The diffraction peak intensities of the (111) crystal plane are 1803, 1304 and 1564, for calcination time of 4 h, 6 h and 8 h respectively; the same condition appeared in diffraction peak intensities of the (311) crystal plane. As can be seen, with a calcination time of 4 h, the characteristic peak intensity and crystallinity are the highest. Moreover, taking into account the economic cost and time cost, the calcination time is 4 h for subsequent experiments.

Figure S6 (b and c) shows the TG curve of precursor nanofibers. The TG thermal behavior of pure PVP was analyzed by precursor nanofibers for NFs@LMO-6:0. Figure S6 (c) TG curve display. The continuous weight loss of NFs@LMO-6:0 precursor nanofibers began at about 55 ℃ and ended at about 500 ℃. Around 100 °C, 400 °C, and 480 °C, we observed three regions of weight loss. The TG curve shows a wide endothermic peak at about 100 °C, which is caused by the loss of water and solvent. The loss of water and solvent is complete at about 400 °C, and the residual mass is approximately 95%; it is attributed to the decomposition of the side chains and main chains of polymer PVP that an exothermic peak is observed at around 437.8 °C. It can be seen that PVP begins to decompose at about 400 ℃, ends at about 480 ℃, and completes decomposition at about 80 ℃; when the temperature reaches 795.6 ℃, it is in the state of heat flow. There is no thermal reaction peak within the heat flow, and also the weight loss doesn't amendment, indicating that PVP has been fully degraded, and the quantity of residual carbon is concerning 15.43%. The mass of metal oxide is defined as the mass of the mixture minus the residual carbon. It is calculated that the

mass of metal oxide accounts for about 25.15wt% of the nanofiber film.

With NFs@LMO-6:12 as an example, the thermal behavior of LMOs precursor nanofibers was analyzed. TG curves showed that the continual weight loss of precursor nanofibers began at regarding 50 °C and all over at regarding 500 °C. Four weight-loss regions were determined at concerning 103 °C, 344.7 °C, 398 °C and 441.8 °C. As shown within the TG curve, the wide endothermic peak at regarding 103 ℃ is taken into account to be the loss of absorbed water. The exothermic peak at regarding 344.7 ℃ is attributed to the decomposition of manganese acetate and the simultaneous formation of transition products of $Li_{1.6}Mn_{1.6}O_4$. The reaction equations are shown in equations 1, 2 and 3; the exothermic peaks at 398 ℃ and 441.8 ℃ were attributed to the degradation of the PVP aspect chain and main chain as well as the decomposition of metallic element salt ($LiClO_4$), respectively. The transition product chemical transformations occur and began to transform into the spinel-type $Li_{1.6}Mn_{1.6}O_4$. The reaction equations are shown in equations 4 and 5. The weight loss does not change in the heat flow at temperatures higher than 500 °C, this indicates that PVP has been fully degraded, and pure spinel-type $Li_{1.6}Mn_{1.6}O_4$ has been prepared. At this moment, the residual mass is a mixture of metal oxide and a small amount of carbon residue, and the residual amount is about 40.58%. The prominent diffraction peak in the XRD pattern further supports this theory (Figure S6 d).

Reaction equation in the electrospinning stage:

The first step: $Mn(CH_3COO)_2 \cdot 4H_2O = Mn(OH)_2 + 2CH_3COOH + 2H_2O$ (1)

The second step: $Mn(OH)_2 = MnO + H_2O$ (2)

The reaction equation of the calcination stage:

The first step (< 400 ℃): $6MnO + O_2 = 2Mn_3O_4$ (3)

The second step (> = 400 ℃): $LiClO_4 = LiCl + 2O_2$ (4)

The third step: $Mn_3O_4 + LiCl + O_2 \rightarrow Li_{1.6}Mn_{1.6}O_4$ (5)

The images at different calcination temperatures are shown in Figure S6 (e ~ g). In the process of structural change of fibers prepared from polymer and metal salt double precursors. Mn_3O_4 grains are first crystallized from amorphous Mn $(CH_3COO)_2 \cdot 4H_2O$, dispersed and fixed in amorphous $LiClO_4$. When $LiClO_4$ begins to crystallize at a higher temperature, the subsequently formed grains adhere to the pre-existing grains. At a certain stage, the fiber presents a network structure similar to that before calcination (Figure S6 e ~ g). However, with the increase in temperature, a large amount of $Li_{1.6}Mn_{1.6}O_4$ grains crystallize continuously and gradually fill the gap left by volatiles. $Li_{1.6}Mn_{1.6}O_4$ nanofibers with dense grain structure were obtained by calcination after crystallization. As a result, follow-up tests were carried out at 500 °C. Introduces the evolution process of the lithium-ion sieve precursor during heat treatment (Figure S7).

S11 Characterization of lithium-ion sieve

Taking the precursor nanofibers prepared from NFs@LMO-6:6 spinning solution as an example, XPS characterization of a sample was carried out, and the valence analysis of Mn in NFs@LMO-6:6 was carried out through XPS characterization. Figure S8 (a) showed the XPS full spectrum of NFs@LMO-6:6. The results show that the sample is composed of elements Li, Mn, O and C. The Mn 2P and Mn 3S spectra of the sample are shown in Figures 2 (a) and (b) (In Manuscript), respectively. The binding energies

of Mn^{4+} Mn2p3 peaks are approximately 641.82 eV and 642.91 eV, and the electronic binding energies of Mn^{4+} Mn 2p1 are approximately 653.46 eV and 654.45 eV. The binding energy of Mn^{3+} Mn2p3 electrons is about 640.69 eV, and the binding energy of Mn^{3+} Mn 2p1 electrons is about 652.2 eV. The results showed that the sample contains 11.26% Mn^{3+} and 88.74% Mn^{4+}, and the average valence of Mn is calculated to be $Mn^{3.89+}$, the average valence of Mn is lower than the theoretical valence (Mn^{4+}), but it is close to Mn^{4+}. The reason is that the electrospinning method may not fully react during the high-temperature calcination to remove PVP and the crystallization process, resulting in a decrease in product purity.

To explore the adsorption mechanism of the prepared adsorbent, infrared characterization was used to explain it. Figure S9 (a) shows that the absorption peaks near 640 cm^{-1} and 520 cm^{-1} are due to characteristic vibration peaks of Mn-O and Li-O, respectively indicating that the lithium manganese oxide lithium-ion sieve precursor is successfully prepared. After the addition of polymer increased from 6wt% to 9wt%, the infrared peak positions were the same, but the characteristic vibration peaks of Mn-O and Li-O were weakened after the addition of polymer increased, indicating that the addition of polymer increased could result in characteristic vibration peaks of Mn-O and Li-O are partially covered. The reason can be attributed to the fact that when the added amount of polymer is 9wt%, after the two-step treatment of electrospinning and high-temperature calcination, the residual amount of carbon is higher than that of the polymer is 6wt% added. When the amount is 6wt%, it forms a composite material of lithium manganese oxide and carbon residue, which weakens the characteristic

vibration peaks of Mn-O and Li-O. Overall, it is indicated that the most suitable polymer addition amount is 6wt%. To explore the structural stability of the nanofiber lithium-ion sieve, infrared characterization was carried out on the recycled lithium-ion sieve. The polymer addition amount was 6wt%, and the metal salt addition amount was 6wt%.

Two steps were required to prepare the precursors for lithium-ion sieves. The recovered sample was tested after being treated with 0.5 $mol \cdot L^{-1}$ HCl, adsorbing in 100 $mg \cdot L^{-1}$ lithium, and then desorbing. Between each step, samples washed to neutrality with ultrapure water. The samples tested in simulated brine were recovered using the same method. The two recovered samples are named NFs@LIS-6:6-A and NFs@LIS-6:6-B in Figure S9 (a). The results show that the peak position of the lithium-ion sieve after the acid recovery treatment is the same as that of the precursor before use, but for the lithium-ion sieve after pickling, the lattice coupling vibration of H protons appears near 910 cm^{-1}, This indicated that Li^+-H^+ ion-exchange reaction occurs during the acid leaching process, in this process, Li^+ dissolves from the spinel skeleton while H^+ enters the crystal lattice, and then the precursor transformation into lithium-ion sieves. It is proved that the adsorption mechanism of the adsorbent is the Li^+-H^+ ion-exchange mechanism.

Figure S9 (c) showed that the N_2 adsorption-desorption curve and the pore size distribution of NFs@LMO-9:6 porous nanofibrous. The isotherms were identified as type IV, which indicated that the sample was porous material and that was classified as a few porous nanofibrous exhibiting an unique sorption isotherm due to unique

structure. NFs@LMO-9:6 porous nanofibrous show microporous structures of three different pore diameters of 69.29 Å, 88.24 Å and 155.41 Å, which was revealed by pore size distribution in Figure S9 (d). In addition, the NFs@LMO-9:6 porous nanofibrous has a Langmuir specific surface area, BET surface area and a BJH adsorption cumulative of pore volume with 97.22 $m^2 \cdot g^{-1}$, 8.875 $m^2 \cdot g^{-1}$ and 0.059 $cm^3 \cdot g^{-1}$, independently.

S12 Adsorption kinetics and isotherms

Figure S10 (a) is a graph showing the adsorption capacity of lithium-ions on a lithium-ion sieve at different times. As shown in the figure that the adsorption of lithium-ions on the lithium-ion sieve has a trend of first being fast and then slow. The front adsorption is faster because the surface of the spinel-like lithium-ion sieve directly contacts the lithium-containing solution and adsorbs Li^+ in the adsorption solution, the rate is very fast; but the internal active sites with adsorption capacity need the surface Li^+ to migrate inward, this process is relatively slow, and the late in the adsorption process, due to the increase of the Li^+ migration distance, the adsorption capacity will increase in a long time. Similarly, Li^+ migration to the inside also requires driving force, even so, the adsorption capacity is still slowly increasing after 40 minutes due to the low concentration of Li^+ in the solution. However, the increase in adsorption capacity after 40 min is relatively small. In summary, a rapid increase in adsorption capacity of the NF@LIS-6:6 adsorbent was observed in the first 40 minutes, followed by a gradual increase slowly occurred until the equilibrium was reached after 60 minutes. The adsorption equilibrium is reached in a shorter time. This is because NF@LIS-6:6 has a

porous nanofiber structure imitating the loofah skeleton, which contains high porosity and exposes more adsorption sites. These factors promote the contact between adsorption sites and lithium-ion.

To fit the adsorption data of nanofiber morphology $H_{1.6}Mn_{1.6}O_4$, the pseudo-first-order kinetic and pseudo-second-order kinetic models were used. Figure S10 (b and c) and Table S3 present the results. The NF@LIS-6:6 adsorbent follows the pseudo-second-order kinetic model (R^2>0.99), indicating that the lithium-ion sieve adsorption process is primarily a chemical adsorption process. Furthermore, the adsorption rate constant of 0.0130 $g \cdot mg^{-1} \cdot min^{-1}$ is the highest among the reported manganese-based lithium-ion sieves, indicating that the nanofiber morphology of the lithium-ion sieve has a relatively fast adsorption rate, owing to the porous structure of the morphology, which is more conducive to Li^+ diffusion in the particles. The initial adsorption for 40 minutes showed a good adsorption rate and adsorption capacity, but after 40 minutes, the adsorption capacity gradually stabilized and no significant changes occurred until the adsorption equilibrium is reached.

Figure S10 (d) is a graph of the adsorption capacity of lithium-ions on a lithium-ion sieve at different initial lithium concentrations. With the increase in Li^+ concentration from 18.17 $mg \cdot L^{-1}$ to 200 $mg \cdot L^{-1}$, the Li^+ adsorption capacity of NFs@LIS-6:6 will increase significantly from 17.27 $mg \cdot g^{-1}$ to 37.37 $mg \cdot g^{-1}$, then an equilibrium adsorption state is reached. The high adsorption capacity obtained is attributed to the high density of adsorption sites of NFs@LIS-6:6 and the porous structure of nanofiber morphology.

The adsorption isotherm parameters are summarized in Figure S10 (e and f) and Table S4. The adsorption capacity of NFs@LIS-6:6 increases with the increase of the initial lithium-ion concentration. The regression coefficient (R^2) of the Langmuir model is higher than the regression coefficient (R^2) of the Freundlich model, indicating that the adsorption process of the adsorbent mainly occurs on the surface of the adsorbent. The maximum equilibrium adsorption capacity reaches 37.37 $mg \cdot g^{-1}$, near thermodynamic simulated adsorption capacity (44.64 $mg \cdot g^{-1}$), which is better than most common adsorbents. The remarkable Li^+ adsorption capacity of nanofibers $H_{1.6}Mn_{1.6}O_4$ can be attributed to the following factors: (1) the fiber structure prevents agglomeration of the adsorbent and lowers reaction surface area loss; (2) the porous structure provides freely and easily accessible vacancies.

S13 Adsorption desorption cycle and selectivity performance of lithium-ion sieve

Good reusability is important for qualified adsorbents to work out their feasibleness in industrial applications. Their recyclability of them has been studied through multiple adsorption-desorption experiments. First, the lithium-ion sieve precursor is eluted under dilute hydrochloric acid, and then washed with ultrapure water to neutrality, and then the eluted NFs@LIS-6:6 is placed in the lithium solution. Repeat the above operations to perform regeneration experiments. The results are shown in Figure 3 (a) (In Manuscript). In the first adsorption experiment, the adsorption capacity of NFs@LIS-6:6 adsorbent for lithium is 36.58 $mg \cdot g^{-1}$; in the fifth adsorption experiment, The adsorption capacity for lithium was 34.7 $mg \cdot g^{-1}$, which decreased by only 5.1% compared with the first time. The adsorption capacity of Li^+ decreases slightly with the

increase of the service cycle, but it still maintains 94.86% relative to the original adsorbent in the fifth cycle. After regeneration, the structural stability of the adsorbent was additionally evaluated. As shown in Figure 3 (b) (In Manuscript), when the second cycle, the Mn dissolution loss was >1%, then when additional cycles (below 1% from the third cycle), it had been considerably reduced. These results confirm that NFs@LIS-6:6 can be used for Li^+ adsorption for a long time. It has good recycling and application ability for extracting lithium from salt lake brine.

To evaluate the selective behavior of the NFs@LIS-6:6 adsorbent, selectivity experiments were carried out in simulated brine (pH = 7.3±0.1) containing different metal ions (Li^+, Na^+, K^+, Ca^{2+} and Mg^{2+}), and the Li^+ concentration was relatively other cations (Na^+, K^+ and Mg^{2+}) are lower. The Li^+ adsorption capacity of the adsorbent is most affected by Mg^{2+} because its ionic radius is close to Li^+. Therefore, because the ratio of the concentration of magnesium to lithium in the simulated brine is large, the adsorption capacity of the adsorbent for lithium is reduced. The results are shown in Figure 3 (c and d) and Table S5. Although the initial ion concentrations of competing ions are much higher than that of Li^+, the greater the equilibrium partition coefficient (K_d), the stronger the selective adsorption capacity of the adsorbent for this ion. Compared to competing ions (Na^+ is 0.1351 $mL \cdot g^{-1}$, K^+ is 0.3260 $mL \cdot g^{-1}$, Mg^{2+} is 0.4680 $mL \cdot g^{-1}$ and Ca^{2+} is 26.23 $mL \cdot g^{-1}$), Li^+ has a much higher equilibrium distribution coefficient (K_d) (197.33 $mL \cdot g^{-1}$), it shows that the adsorbent has higher selective adsorption capacity for lithium-ion. There is a strong ion sieving effect of the spinel-type $Li_{1.6}Mn_{1.6}O_4$ lattice, which may account for the high adsorption selectivity of Li^+

on NFs@LIS-6:6. Li^+ has a much smaller ionic radius than Na^+, K^+, and Ca^{2+}. The adsorption site of NFs@LIS-6:6 is formed by leaching Li^+ from the spinel-type $Li_{1.6}Mn_{1.6}O_4$, so ions are allowed to enter lithium vacancies only if their radii are smaller than or equal to the Li^+ radius. Mg^{2+} is a multivalent ion with a size comparable to Li^+, the Ionic radius is shown in Table S4. Multivalent ions typically show greater selectivity than monovalent ions. However, adsorption of Mg^{2+} by the spinel-type $H_{1.6}Mn_{1.6}O_4$ is less selective than that for Li^+. With Mg^{2+} hydration energy of -455 $kcal \cdot mol^{-1}$ compared to Li^+ hydration energy of -122 $kcal \cdot mol^{-1}$, the hydration energy of Mg^{2+} is about four times that of Li^+, a higher amount of energy is needed for the dehydration of Mg^{2+} into lithium-ion sieves. The following criteria must be met for adsorption to take place in the ion sieve: (1) the radius of the ions must be equal to or smaller than the size of the cavity of the lithium-ion sieve; (2) A low dehydration energy level is a requirement for dehydration. The adsorption mechanism ais shown in Figure 4 (b) (In Manuscript). The overall results show that NFs@LIS-6:6 can be easily used to capture lithium-ions with high selectivity from water-rich Li^+, Na^+, K^+, Ca^{2+} and Mg^{2+}, such as seawater or salt-lake brine. The adsorption capacity of adsorbent NFs@LIS-6:6 in simulated brine is 32.43 $mg \cdot g^{-1}$. Nevertheless, based on the sieving effect of ion size, the separation factor (α_{Mg}^{Li}) of adsorbent NFs@LIS-6:6 for Mg^{2+} is 421.68, and the lithium-ion sieve has high selectivity to Li^+.

S14 Comparison with literature

The Li^+ adsorption capacity of the nanofiber adsorbent was compared with other particulate manganese series lithium-ion sieves adsorbents. The results are summarized

in Table 1 (In Manuscript) and Figure S11. The nanofiber has a higher Li^+ adsorption performance than the particle-type adsorbent. Generally, as the particle size of the adsorbent decreases, the adsorption capacity of the particulate adsorbent increases. More importantly, the adsorption capacity of the nanofiber $H_{1.6}Mn_{1.6}O_4$ adsorbent (NFs@LIS-6:6) is greater than that of the particulate adsorbent. In particular, compared with particulate adsorbents, The Li^+ adsorption rate and adsorption capacity of NFs@LIS-6:6 were increased by 94.44% and 33.90% respectively, showing the extraordinary potential of extracting Li^+ from salt lake brine. The reason behind this can be explained by the high surface energy of nano-sized particles. Consequently, Particle-to-particle contact reduces the number of adsorption sites because they aggregate in the water phase. In addition, NFs@LIS-6:6 has a porous nanofiber structure and rich lithium-ion adsorption sites. It not only has the small-size effect, excellent heat resistance and chemical stability of inorganic nanomaterials, but also easily form a self-supporting fiber skeleton, avoiding the defects of increasing surface energy and reducing adsorption efficiency caused by the use of traditional particles. Without a doubt, a high aspect ratio of nanofibers results in a one-dimensional structure that reduces the susceptibility of nanofibers to aggregation. The adsorption capacity of NFs@LIS-6:6 nanofibers is higher than that of previously reported manganese-based lithium-ion sieve adsorbents, indicating its superior performance. Therefore, it plays an important role in the field of lithium extraction from salt lakes.

2. Figures

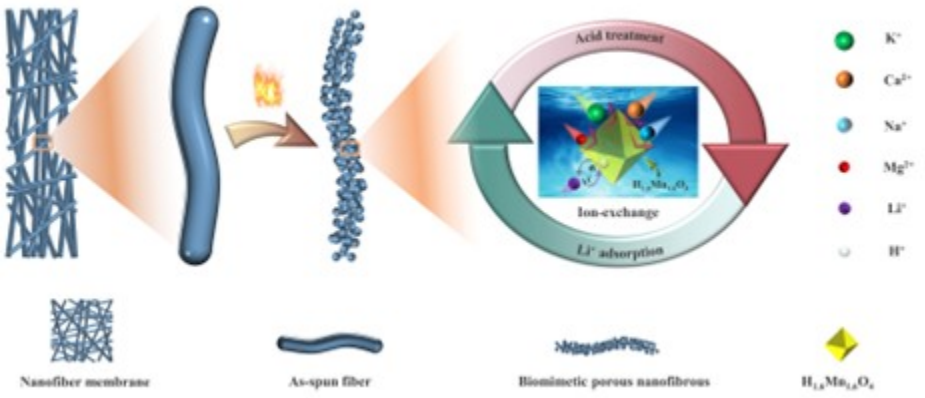

Scheme 1. Schematic illustration of the synthesis of biomimetic porous nanofibrous $H_{1.6}Mn_{1.6}O_4$ and possible high-efficiency and fast selective extraction Li^+ from brine

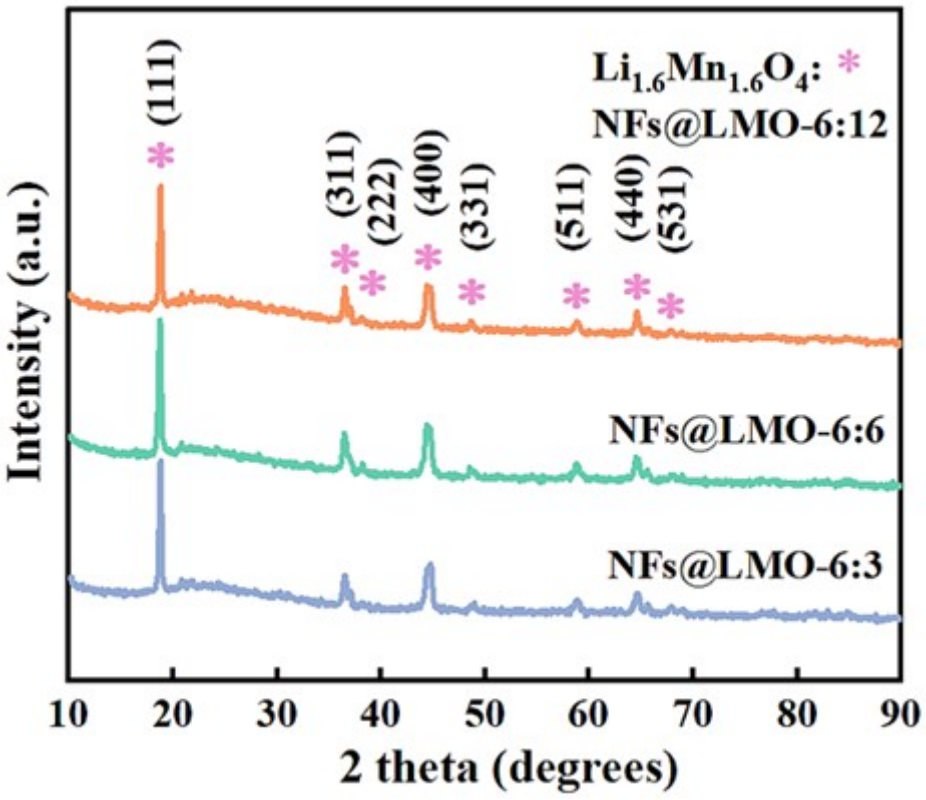

Figure S1. XRD spectra of different polymers: metal salt ratio

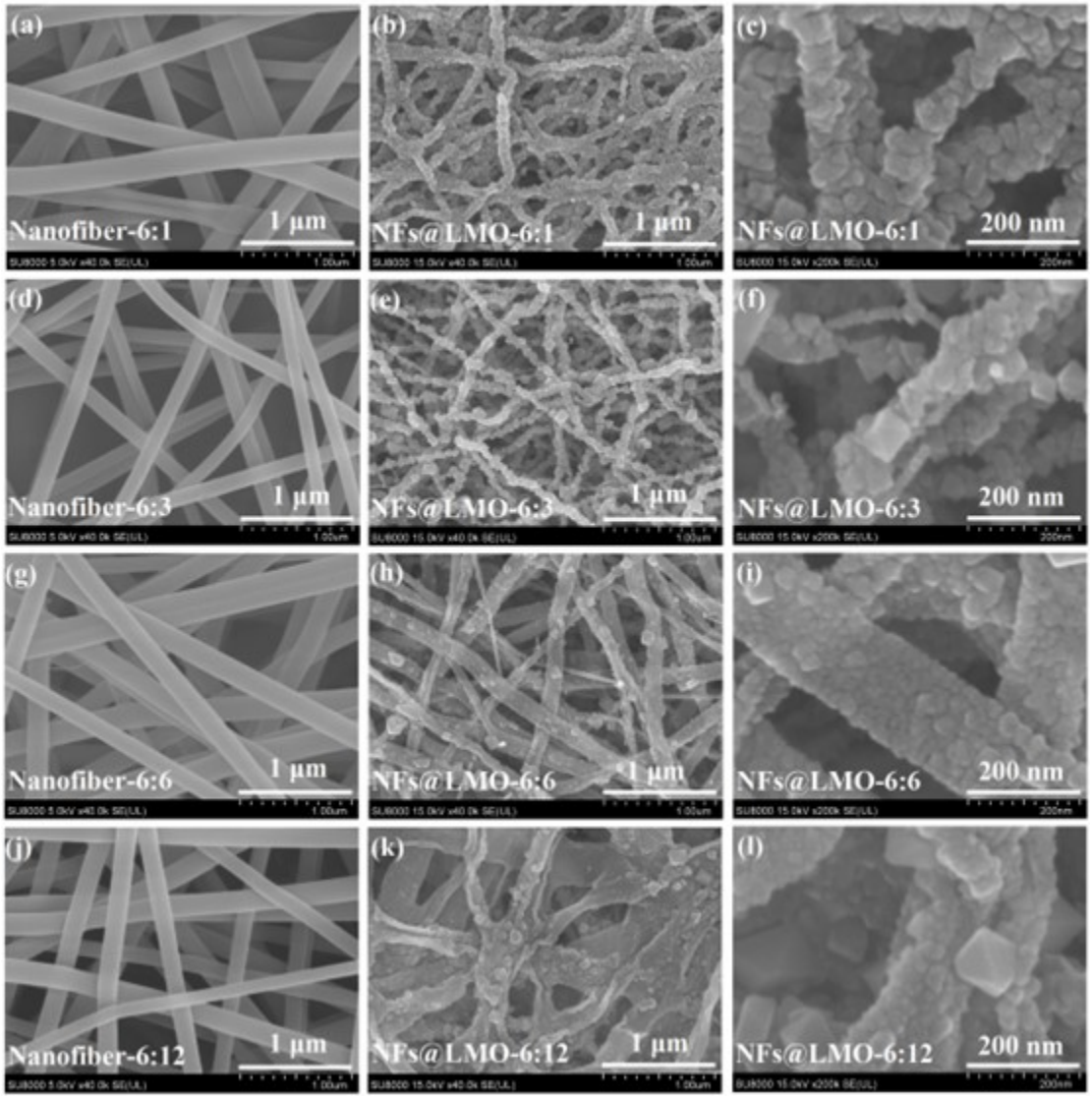

Figure S2. SEM images of nanofibers before and after calcination with metal salt content

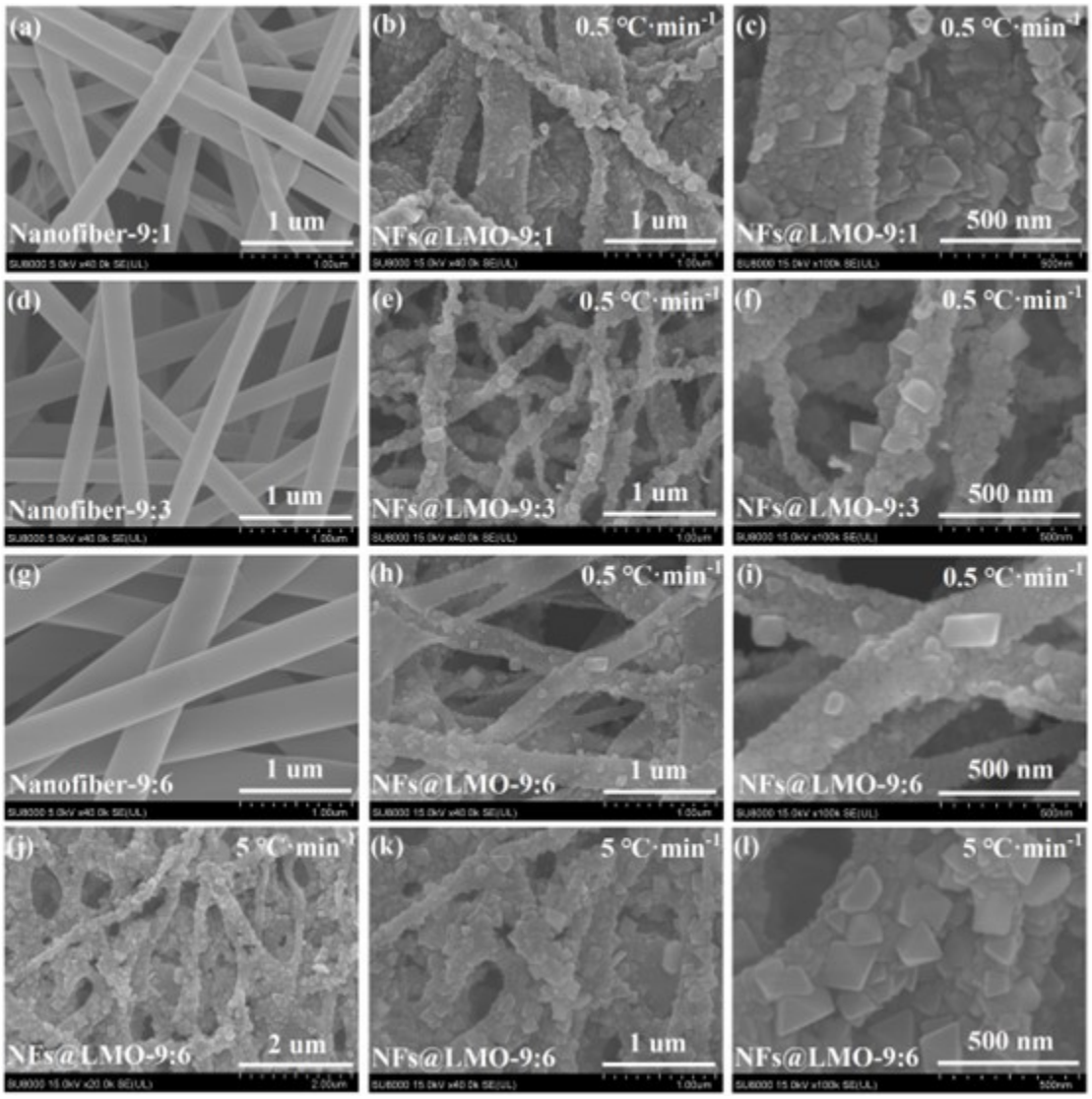

Figure S3. SEM images of nanofibers before and after calcination with different polymers: metal salt ratio

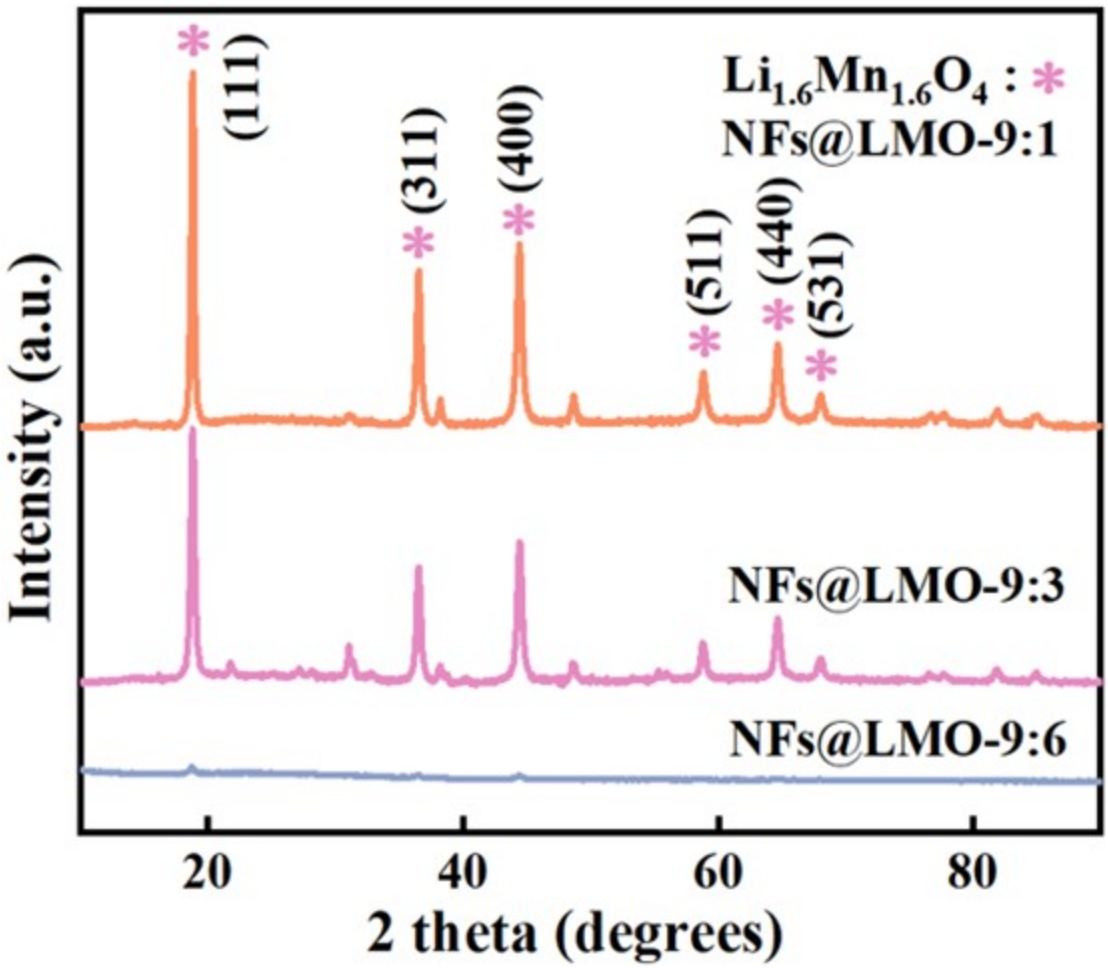

Figure S4. XRD spectra of different polymers: metal salt ratio

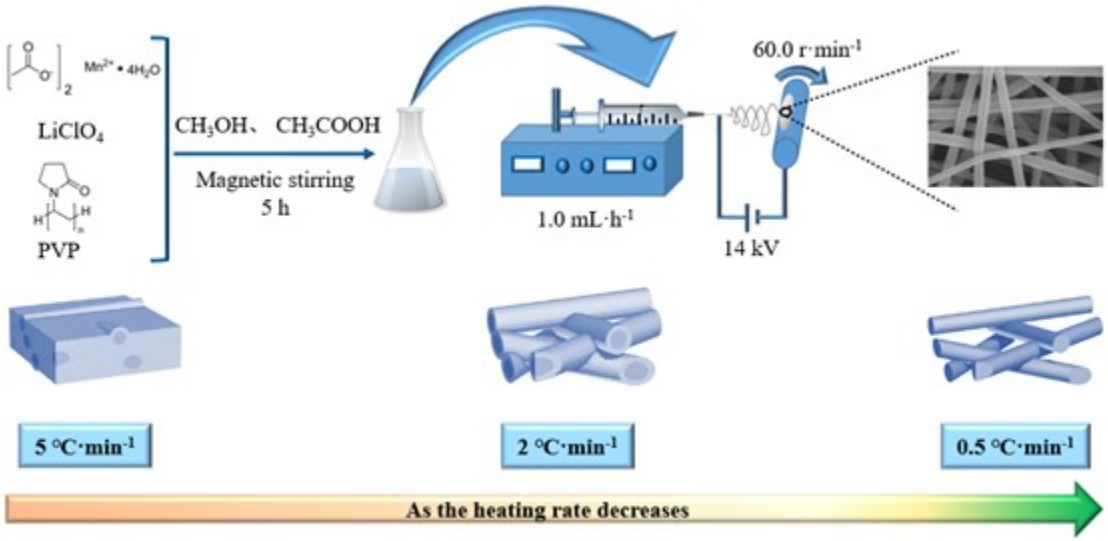

Figure S5. The preparation process with a nanofiber membrane; Schematic diagram of morphology evolution with the decrease of the heating rate

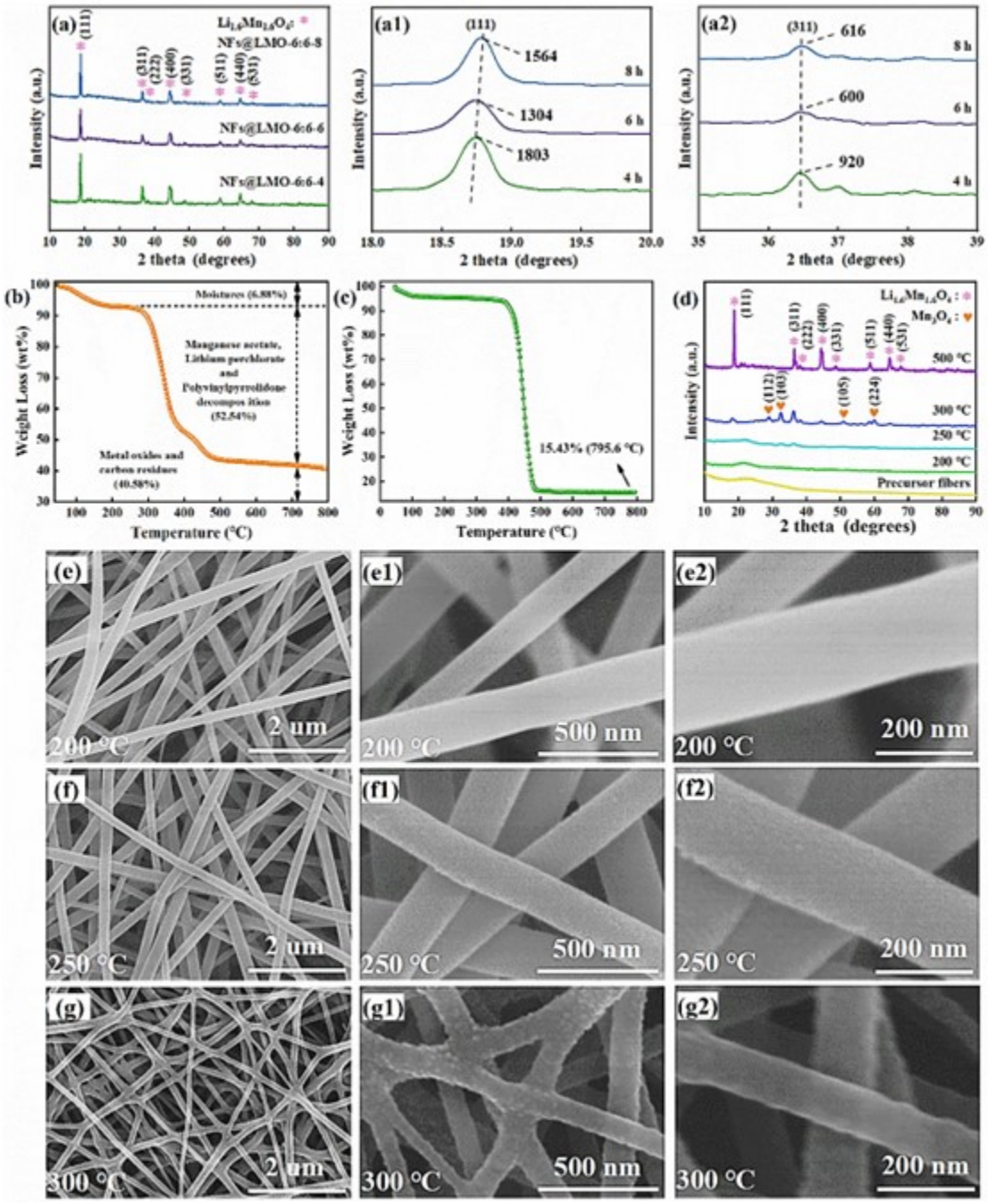

Figure S6. (a) A comparison of the XRD patterns of lithium-ion sieve precursors with different calcination times; (b) The TG analysis of precursor nanofiber with NFs@LMO-6:12; (c) The TG analysis of precursor nanofiber with NFs@LMO-6:0; (d) The XRD patterns of different calcination temperatures; (e ~ g) SEM characterization of calcination temperatures at (e) 200 ℃, (f) 250 ℃ and (g) 300℃

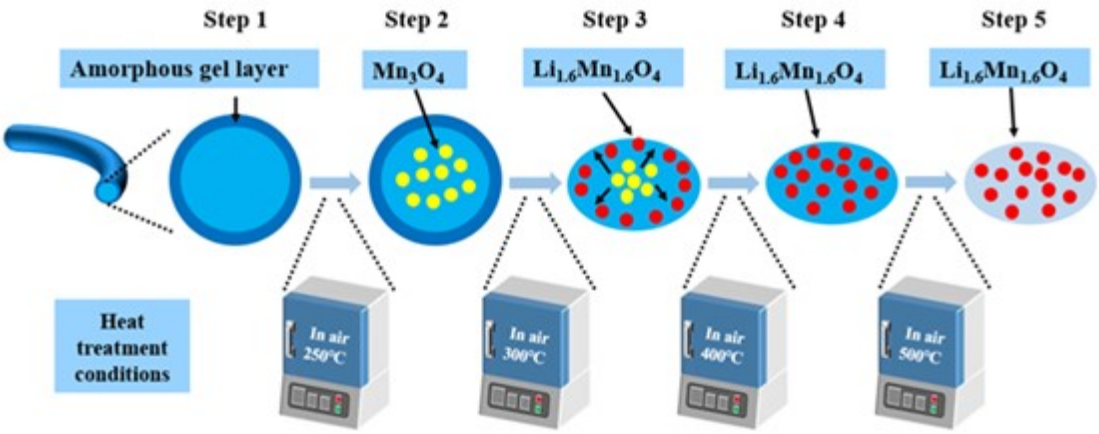

Figure S7. Schematic diagram of the evolution of precursor for lithium-ion sieve during thermal treatment

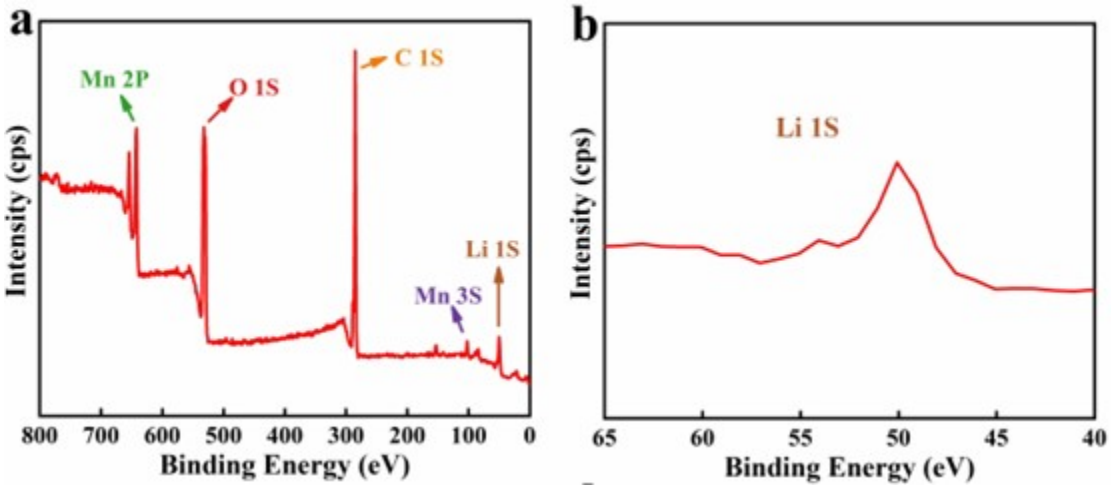

Figure S8. (a) XPS spectra of NFs@LMO-6:6; (b) high-resolution XPS spectra of Li 1S

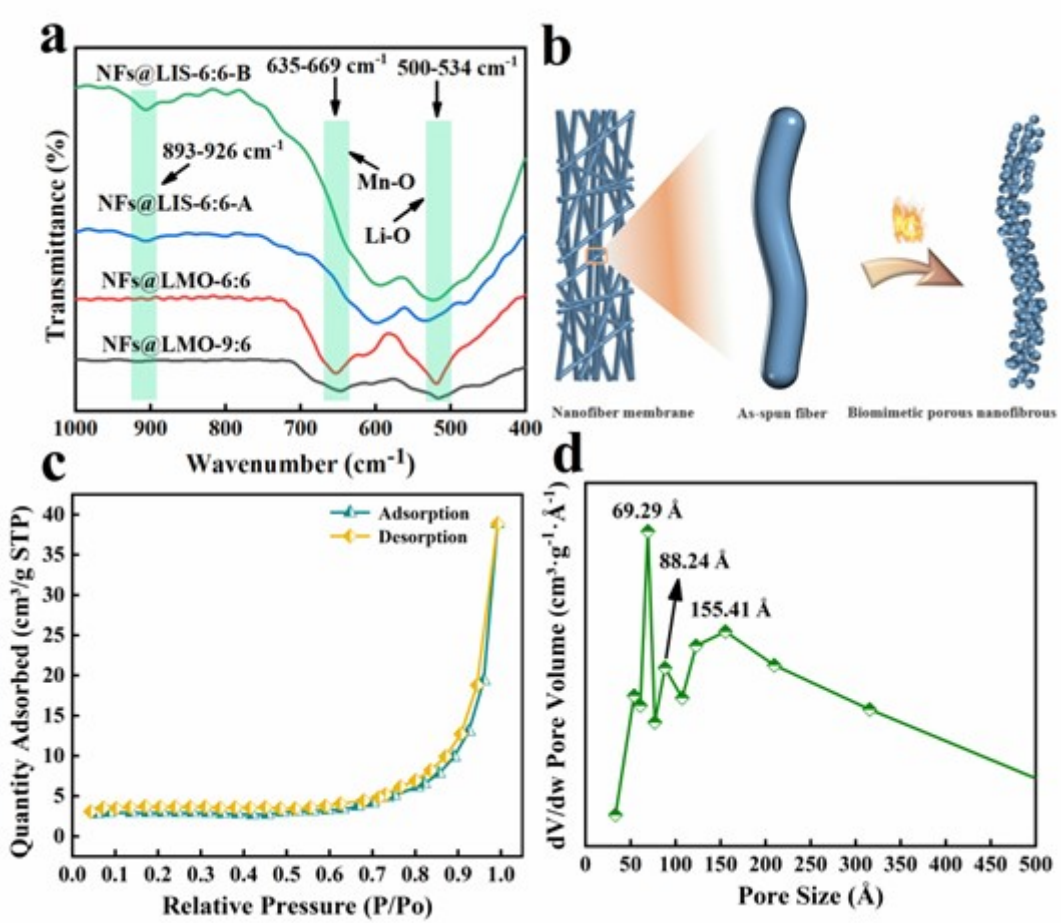

Figure S9. (a) Infrared spectra of NFs@LMO-6:6, NFs@LMO-6:6-A, NFs@LMO-6:6-B and NFs@LMO-9:6; (f) Schematic illustration of the synthesis of biomimetic porous nanofibrous $H_{1.6}Mn_{1.6}O_4$; (c) N_2 adsorption-desorption isotherms; (d) the pore size distribution curve of NFs@LMO-9:6

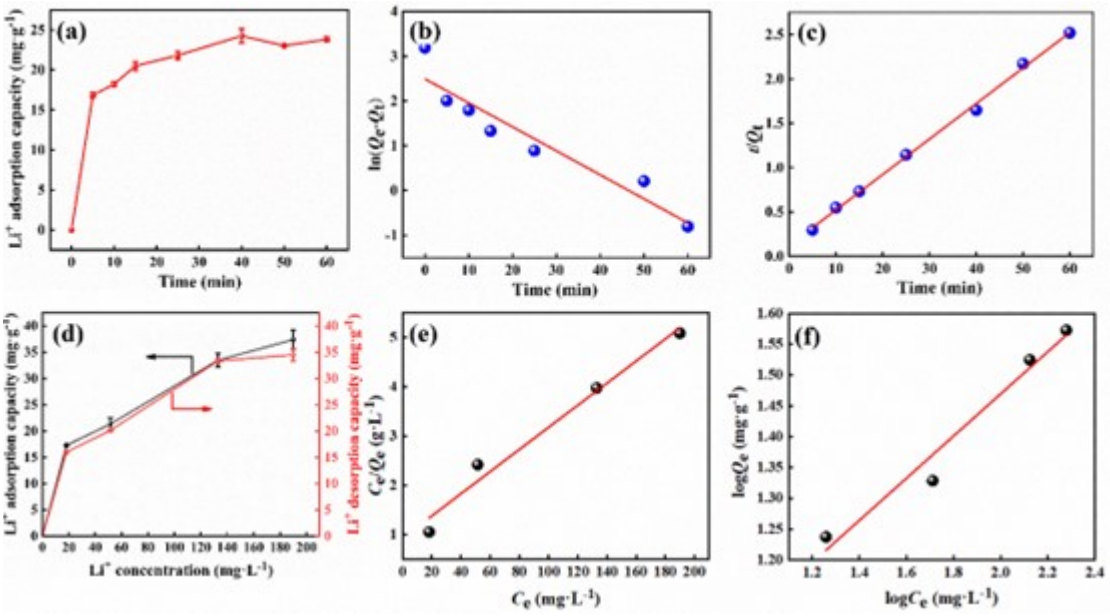

Figure S10. (a) The effect of adsorption time on adsorption performance (C_0=50 mg·L^{-1}, pH=9.8±0.1); (b) Quasi-first-order adsorption kinetics simulation; (c) Quasi-secondary adsorption kinetics simulation; (d) Effect of Li^+ concentration on adsorption and desorption performance of NFs@LIS-6:6 (T=30 °C, pH=9.8±0.1); (e) Langmuir thermodynamic simulation; (f) Freundlich thermodynamic simulation

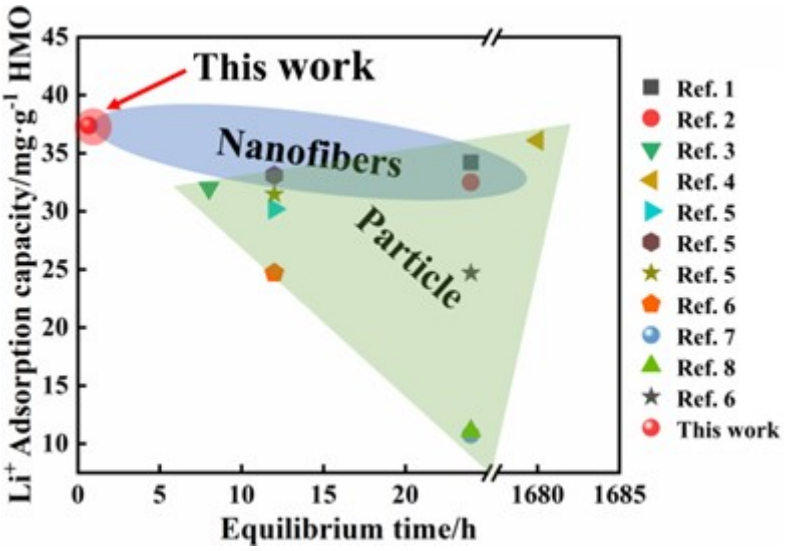

Figure S11. Comparison of adsorption performance of different manganese series lithium-ion

sieves

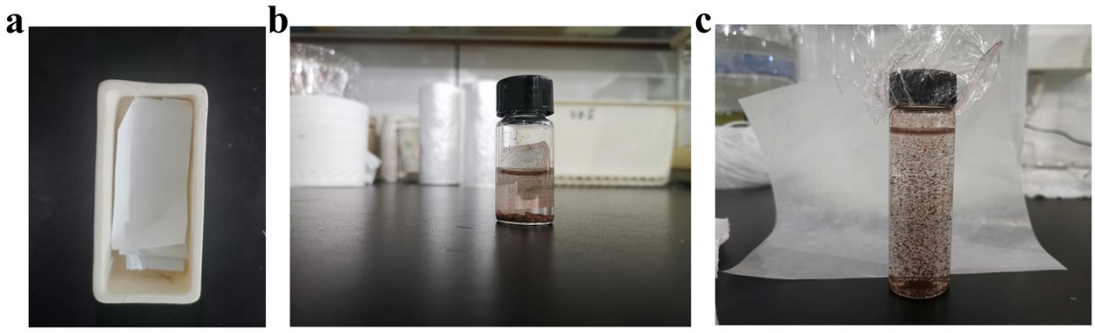

Figure S12. Electronic Photographs. (a) Nanofibers before calcination, (b, c) dispersed in lithium solution after calcination

3. Tables

Table S1. Concentrations of PVP, metallic salt and solvents in mixed solutions

Sample NO.	PVP (wt%)	Metallic salt (wt%)[a]	Solvents (wt%)[b]
NFs@LMO-6:1	6	1	93
NFs@LMO-6:3	6	3	91
NFs@LMO-6:6	6	6	88
NFs@LMO-6:12	6	12	82
NFs@LMO-9:1	9	1	90
NFs@LMO-9:3	9	3	88
NFs@LMO-9:6	9	6	85

[a] Composed of $LiClO_4$ and $Mn(CH_3COO)_2{\cdot}4H_2O$, stoichiometric ratio of 1:1

[b] Composed of methyl alcohol and acetic acid glacial

Table S2. The value of Mn and elemental content analysis for NFs@LMO-6:6

Sample	Manganese content (%)	Z_{Mn}
NFs@LMO-6:6	8.04	3.89

Table S3. The pseudo-first-order kinetic model and the pseudo-second-order kinetic model adsorption kinetic parameters of Li^+ on NFs@LMO-6:6

Absorbents	Pseudo-first-order kinetic model			Pseudo-second-order kinetic model		
	Q_1(mg·g^{-1})	k_1(min^{-1})	R^2	Q_2(mg·g^{-1})	k_2(g·mg^{-1}·min^{-1})	R^2
NF@LIS-6:6	24.26	0.0536	0.9087	25.00	0.0130	0.9977

Table S4. The adsorption equilibrium constants of Langmuir and Freundlich adsorption isotherm equations

Adsorbent	Langmuir model			Freundlich model		
	Q_m(mg·g^{-1})	K_L(L mg^{-1})	R^2	1/n	K_F	R^2
NFs@LIS-6:6	44.64	0.0240	0.9778	0.3423	6.0912	0.9674

Table S5. Selective adsorption property of NFs@LIS-6:6 adsorbent (T=30 °C, t=12 h, pH=7.3±0.1)

Metal Ions	Ionic radius (pm)	C_0 (mg·L^{-1})	Q_e (mg·g^{-1})	K_d (mL·g^{-1})	C_F (×10^{-3} L·g^{-1})	α_{Me}^{Li}
Li^+	76	197.54	32.43	197.33	164.19	1
Na^+	102	2532.8	0.3421	0.1351	0.135	1460.67
K^+	138	1259.9	0.4106	0.3260	0.326	605.37
Ca^{2+}	100	37.50	0.9580	26.23	25.55	7.52
Mg^{2+}	72	10700.0	5.005	0.4680	0.468	421.68

Table S6. Comparison of adsorption performance of different manganese series lithium-ion sieves

Adsorbent	Raw material	Morphology	Li^+ solution	Equilibrium time	Li adsorption capacity/mg·g^{-1}	Manganese dissolution/wt%	Ref.
$H_{1.6}Mn_{1.6}O_4$	$Mn(CH_3COO)_2·4H_2O$/ $LiClO_4$	Nanofibers	LiCl solution/Brine (Li^+ 200 mg·L^{-1}, pH = 9.8±0.1, 12 h/Li^+ 197.54 mg·L^{-1}, pH = 7.3±0.1, 12 h)	40 min	37.37/32.43	0.83	This work
$H_{1.6}Mn_{1.6}O_4$	γ-MnOOH/LiOH	Irregular particle	Seawater（Li^+ 5 mg·g^{-1}, pH=8, 6 days）	6 days	37	1.5	9
$H_{1.6}Mn_{1.6}O_4$	γ-MnOOH/LiOH	Irregular particle	Seawater（Li^+ 0.17 mg·g^{-1}, pH=8, 4 weeks）	4 weeks	36.1	2.5	4
$H_{1.6}Mn_{1.6}O_4$	-	-	Brine (Li^+ 1600 mg·L^{-1}, pH=6.6, 8 h)	8 h	32	0.5	3
$H_{1.6}Mn_{1.6}O_4$	($KMnO_4$, $MnCl_2$)/LiOH	Irregular particle	Salt lake (Li^+ 1.79×10^4 mg·L^{-1}, pH=6.4, 48 h)	48 h	28.6	1.2	10
$H_{1.6}Mn_{1.6}O_4$	γ-MnOOH/$LiOH·H_2O$	Rod-like	Brine (Li^+ 182 mg·L^{-1}, pH =	12 h	30.20	2.2	5

			8, 12 h)				
$H_{1.6}Mn_{1.6}O_4$	$MnCO_3/LiNO_3$	Spherical	Brine (Li^+ 182 mg·L^{-1}, pH = 8, 12 h)	12 h	33.10	1.6	5
$H_{1.6}Mn_{1.6}O_4$	$MnO/LiOH·H_2O$	Flower-like	Brine (Li^+ 182 mg·L^{-1}, pH = 8, 12 h)	12 h	31.47	2.4	5
$H_{1.6}Mn_{1.6}O_4$	$Mn(CH_3COO)_2·4H_2O/LiNO_3$	3D macroporous-mesoporous	Brine (Li^+ 182 mg·L^{-1}, pH = 8, 12 h)	12 h	42.15	3.5	5
HMn_2O_4	$Mn(CH_3COO)_2·4H_2O/LiNO_3$	Nanofibers	Mixed solution of LiCl and LiOH (Li^+ 200 mg·L^{-1}, pH = 11, 24 h)	24 h	34.21	-	1
HMn_2O_4	$Mn(CH_3COO)_2·2H_2O/LiNO_3$	Nanofibers	Li solution/Seawater (Li^+ 100 mg·L^{-1}/Li^+ 0.17 mg·L^{-1}, pH = 8, 24 h)	24 h	32.50/18.81	-	2
HMn_2O_4	$Mn(NO_3)_2/LiOH$	Particle	Li solution (Li^+ 69.41 mg·L^{-1}, pH = 10.10, 72 h)	24 h	20.47	-	11
$H_{1.6}Mn_{1.6}O_4$	$Mn(NO_3)_2·4H_2O$/ $LiOH·H_2O$	Particle	LiCl solution (Li^+ 6.08 mg·L^{-1}, pH = 12, 48 h)	4 h	24.7	-	6

Table S7. Compositions of artificial brine ($mg \cdot L^{-1}$)

	Li^+	Na^+	K^+	Ca^{2+}	Mg^{2+}
Brine	197.54	2532.8	1259.9	37.50	10700.0

References

1. S. Choi, G. Hwang, S. Ilyas, Y. Han, N.V. Myung, B.C. Lee, Y. Song and H. Kim, *Sep. Purif. Technol.*, 2020, 242, 116757.
2. Y. Han, S. Kim, S. Yu, N.V. Myung and H. Kim, *J. Ind. Eng. Chem.*, 2020, 81, 115-123.
3. R. Chitrakar, Y. Makita, K. Ooi, A. Sonoda, *Chem. Lett.*, 2012, 41, 1647-1649.
4. R. Chitrakar, H. Kanoh, Y. Miyai and K. Ooi, *Ind. Eng. Chem. Res.*, 2001, 40, 2054-2058.
5. X. Li, B. Tao, Q. Jia and R. Guo, *Chin. J. Chem. Eng.*, 2021, 34, 68-76.
6. L. Liu, H. Zhang, Y. Zhang, D. Cao and X. Zhao, *Colloids Surf. A Physicochem. Eng. Asp.*, 2015, 468, 280-284.
7. M.J. Park, G.M. Nisola, A.B. Beltran, R.E.C. Torrejos, J.G. Seo, S.P. Lee, H. Kim and W.J. Chung, *Chem. Eng. J.*, 2014, 254, 73-81.
8. X. Shi, D. Zhou, Z. Zhang, L. Yu, H. Xu, B. Chen and X. Yang, *Hydrometallurgy*, 2011, 110, 99-106.
9. R. Chitrakar, H. Kanoh, Y. Miyai, K. Ooi, *Chem. Mater.*, 2000, 12, 3151-3157.
10. X. Yang, H. Kanoh, W. Tang, K. Ooi, *J. Mater. Chem.*, 2000, 10, 1903-1909.
11. Q. Zhang, S. Li, S. Sun, X. Yin and J. Yu, *Chem. Eng. Sci.*, 2010, 65, 169-173.